Nanoscale

PAPER

View Article Online
View Journal | View Issue

Cite this: *Nanoscale*, 2019, **11**, 6206

Solvent exfoliation stabilizes TiS_2 nanosheets against oxidation, facilitating lithium storage applications†

Victor Vega-Mayoral,*[a,b] Ruiyuan Tian,[a,b] Adam G. Kelly,[a,b] Aideen Griffin,[a,b] Andrew Harvey,[a,b] Mino Borrelli,[a,b] Katharina Nisi,[a,b] Claudia Backes[c] and Jonathan N. Coleman *[a,b]

Received 22nd November 2018,
Accepted 1st March 2019

DOI: 10.1039/c8nr09446b

rsc.li/nanoscale

Titanium disulfide is a promising material for a range of applications, including lithium-ion battery (LIB) anodes. However, its application potential has been severely hindered by the tendency of exfoliated TiS_2 to rapidly oxidize under ambient conditions. Herein, we confirm that, although layered TiS_2 powder can be exfoliated by sonication in aqueous surfactant solutions, the resultant nanosheets oxidise almost completely within hours. However, we find that upon performing the exfoliation in the solvent cyclohexyl-pyrrolidone (CHP), the oxidation is almost completely suppressed. TiS_2 nanosheets dispersed in CHP and stored at 4 °C in an open atmosphere for 90 days remained up to 95% intact. In addition, CHP-exfoliated nanosheets did not show any evidence of oxidation for at least 30 days after being transformed into dry films even when stored under ambient conditions. This stability, probably a result of a residual CHP coating, allows TiS_2 nanosheets to be deployed in applications. To demonstrate this, we prepared lithium ion battery anodes from nano : nano composites of TiS_2 nanosheets mixed with carbon nanotubes. These anodes displayed reversible capacities (920 mA h g^{-1}) close to the theoretical value and showed good rate performance and cycling capability.

Introduction

Two-dimensional (2D) materials have generated much interest in recent years partly due to their potential for use in a range of applications, including supercapacitors[1–3] and battery electrodes.[4–9] Although graphene[10,11] is undoubtedly the most well-known and widely used 2D material, many others exist, with transition metal dichalcogenides (TMDs) being probably the most known family of inorganic 2D materials.[12] TMDs such as MoS_2 and WS_2 have been thoroughly studied over the last few years, performing well in a wide range of applications including battery electrodes,[13] light modulators[14] and multibit memory.[15] However, not all TMDs are so well-known. For example, titanium disulfide is a less-celebrated member of the TMD family. Although it has recently been utilized in applications including non-linear optical devices[16] and thermoelectrics[17] and has long been proposed as a lithium ion storage material,[18–21] TiS_2 suffers from a significant disadvantage: its low oxidative stability under ambient conditions.[22,23] As a result, this promising material has not yet reached its full potential.

Like most TMDs, TiS_2 can be found in either the 1T or 2H crystalline structure with the 1T polymorph as the most stable phase.[24–26] While TiS_2 is a semimetal in bulk or few-layer form, the electronic band structure of monolayer 1T-TiS_2 is controversial, with some authors claiming the opening of a small bandgap (0.67 eV) in pristine 1T-TiS_2 monolayer.[27] Exfoliated, few-layer TiS_2 dispersions have previously been obtained by both lithium intercalation[28] and liquid phase exfoliation.[23] However, the problem of degradation by oxidation has always been present[23,29] and has largely prohibited the investigation of this material. TiS_2 degrades rapidly in the presence of oxygen or water releasing hydrogen sulfide and converting the TiS_2 to various titanium oxides.[23] Apart from the poisonous, corrosive and flammable nature of H_2S gas,[30] this lack of stability is obviously a huge issue which needs to be addressed.

While encapsulation and working inside a dry-box have been used to get around this problem,[20,31] a simpler solution would of course be welcome. Herein, we report, for the first

[a]*CRANN & AMBER Research Centers, Trinity College Dublin, Dublin 2, Ireland. E-mail: colemaj@tcd.ie, vegamayv@tcd.ie*
[b]*School of Physics, Trinity College Dublin, Dublin 2, Ireland*
[c]*Chair of Applied Physical Chemistry, University of Heidelberg, Im Neuenheimer Feld 253, 69120 Heidelberg, Germany*
†Electronic supplementary information (ESI) available. See DOI: 10.1039/c8nr09446b

time to our knowledge, the exfoliation and size selection of TiS_2 in an open atmosphere at room temperature in such a manner that degradation has been neutralized. The resultant dispersions are stable for months and have been used to prepare battery anodes with high capacity and cycle-ability.

Results and discussion

Exfoliation of TiS_2 in aqueous surfactant solutions

Before attempting at producing a stable dispersion of TiS_2 nanosheets, it is necessary to assess the degradation of exfoliated TiS_2. To do this, we have exfoliated TiS_2 in an aqueous environment, namely a solution of the surfactant sodium cholate (SC). Briefly, TiS_2 powder was added to 14 ml of water and sodium cholate (the starting concentrations were C_{SC} = 2 g L^{-1} and C_{TiS_2} = 20 g L^{-1}) and was sonicated for one hour using a tapered tip at 30% power. The dispersion was not centrifuged but placed in a fridge (~4 °C) and its evolution over time was observed. Fig. 1A shows the oxidation and subsequent phase separation occurring over time. The as-prepared dispersion was a homogeneous, dark-purple liquid (Fig. 1A). Over time, the color of the dispersion's upper section became lighter while the bottom retained the same dark color. By day 20, the dispersion has undergone an evident phase separation with milky material at the top and dark purple/black material in the bottom.

To characterize the nature of this change, Raman spectroscopy (λ_{exc} = 532 nm) has been performed on both the top and bottom sections of the liquid over time by carefully extracting droplets with a pipette, which were then deposited on a substrate for analysis. The Raman spectrum from the bottom section of the dispersion was identical to the spectrum of the starting TiS_2 powder (see the ESI†) containing three resonances at 210, 333 and 380 cm^{-1} and did not change with time (Fig. 1B). The first two modes can be assigned to the E_g and A_{1g} modes, respectively. The third resonance has previously been assigned to defects,[32] and is visible as a shoulder on the high-wavenumber side of the A_{1g} resonance. Conversely, the Raman spectra associated with the top fraction display four new resonances (Fig. 1C and the ESI†) (151, 217, 435 and 471 cm^{-1}), which evolve in intensity over time. While the resonance at ~150 cm^{-1} is present in rutile, anatase and Brookite TiO_2,[33] the remaining resonances do not match those reported from either TiO_2 (in any of its 3 polymorphisms) or Ti_2O_3.[34] However, electron energy loss spectroscopy performed by Long *et al.* reported the presence of Ti^{3+} and Ti^{4+} ions in TiS_2 flakes, which had degraded in aqueous and ambient environments, suggesting the formation of intermediary non-stoichiometric titanium oxides.[23] The ratio of the intensity of the peak at 475 cm^{-1} to the intensity of the main TiS_2 peak (333 cm^{-1}) shows the fraction of degradation product in the top section of the dispersion to increase steadily over time (Fig. 1D).

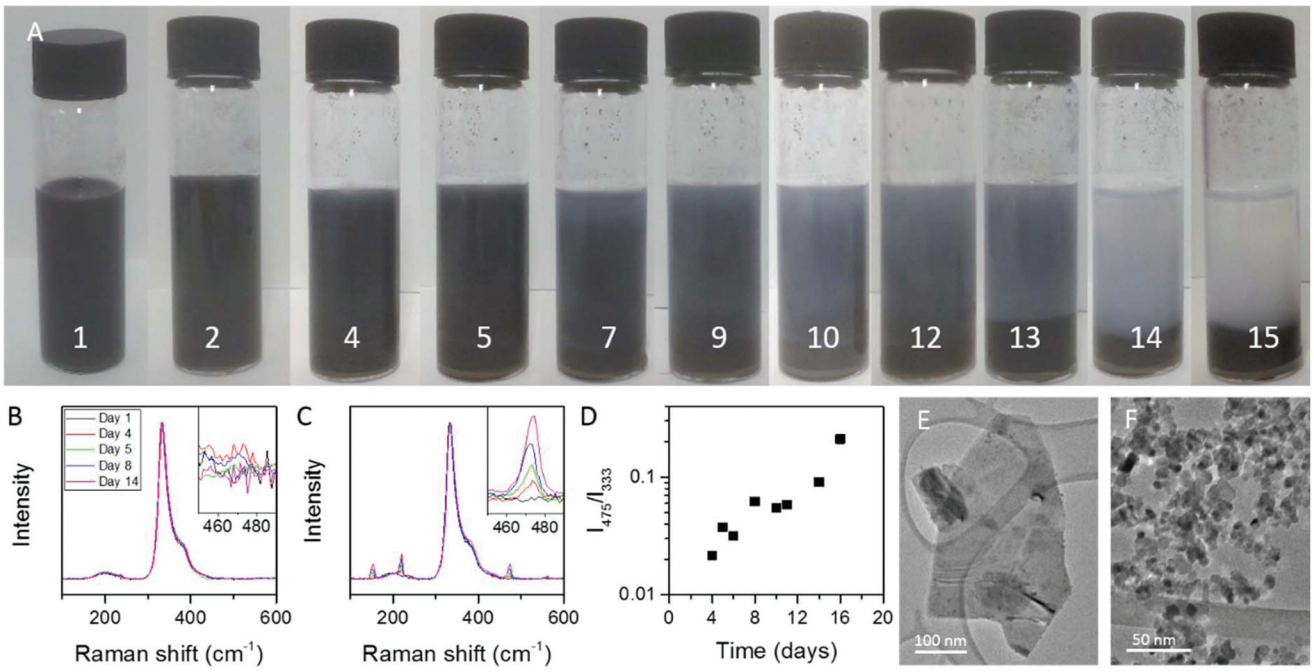

Fig. 1 (A) Photographs of water/surfactant dispersions of liquid-exfoliated TiS_2 taken at various times after exfoliation. The numbers below the vials indicate the number of days after exfoliation. (B–C) Evolution of Raman spectra of (B) the lower portion (always black) and (C) the upper portion (becoming white over time) as a function of time. (D) Ratio of the Raman intensity of the resonance at 475 cm^{-1} to that at 333 cm^{-1}, plotted *versus* time after preparation showing the rise in the TiO_2 component *versus* the TiS_2 component. (E–F) TEM images of typical particles extracted from (E) the lower black portion and (F) the upper white portion of the dispersion on 20th day after exfoliation.

Once the phase separation was completed (*i.e.* after 20 days), TEM was performed on nanosheets extracted from both the white upper and the dark lower sections of the dispersion (Fig. 1E and F). It is clear that the dark part of the dispersion, which shows an exclusively TiS_2 Raman signal, is composed of large 2D flakes and unexfoliated crystallites. Conversely, the white part of the dispersion, where the new Raman resonances are present, is composed of small (~10 nm) particles.

We believe that there are two processes behind this separation; on the one hand, we have the faster sedimentation of larger TiS_2 particles. On the other, we have the oxidation of the smaller TiS_2 nanosheets to give small non-absorbing particles, which remain in the upper portion of the dispersion. These small particles appear to have completely oxidized. However, the larger 2D particles retain much of their TiS_2 characteristics and may only have oxidized partially, suggesting a limit in the penetration depth of oxygen atoms inside the flakes.

Size selection of surfactant-exfoliated TiS_2 nanosheets

To explore this oxidation process in more detail, we produced a second stock dispersion of TiS_2 nanosheets in an aqueous sodium cholate solution and performed a liquid cascade centrifugation protocol[35] both to remove unexfoliated material and to obtain fractions containing flakes of different sizes. To achieve this, the stock dispersion was centrifuged at 1000 rpm for 90 minutes, the sediment discarded and the supernatant then centrifuged again at 3000 rpm. The second sediment was redispersed in 14 mL of water and SC (C_{SC} = 2 g L^{-1}) and the supernatant was centrifuged at 5000 rpm. This procedure was repeated at 7000, 9000 and 12 000 rpm. Using this protocol, the sediments contain nanosheets of different sizes and can be redisposed in SC/water to generate size selected fractions.

TEM analysis has been performed in each of the size-selected dispersions with the sample image (extracted from the 3000–5000 rpm fraction) shown in Fig. 2A (N.B. TEM must be performed quickly to image the nanosheets before any significant oxidation occurs). Statistical analysis of the nanosheet length (the longest axes) yielded the expected log-normal distributions (the histogram of the fraction of flakes trapped between 3 and 5 krpm can be observed in Fig. 2B). The nanosheets' average lateral size ($\langle L \rangle$) changes significantly on increasing the centrifugation speed, as shown in Fig. 2C.

UV-Vis extinction spectra were measured very quickly after exfoliation for the different fractions (Fig. 2D), with a clear size dependence observed. From the second derivative spectra[35] (see the ESI†), 4 different resonances have been identified for each spectrum. Each of these transitions tend to blue shift as the flakes become smaller (the ESI†). Such behavior has been previously observed in other TMDs such as MoS_2 and WS_2,[35,36] and indicates changes in the band structure as well as excitonic screening as the layer number diminishes.

We also measured extinction spectra for each dispersion at different times after exfoliation. For each fraction, the main spectral feature, visible at ~2.2 eV, falls in intensity over time while the extinction in the ultraviolet region (~5 eV) increases over time (Fig. 2E). This behavior is consistent with the transformation of TiS_2 into an oxide with dominant absorption in the UV. We believe the data indicate a continuous reduction in the TiS_2 content and an increase in the presence of titanium oxides.

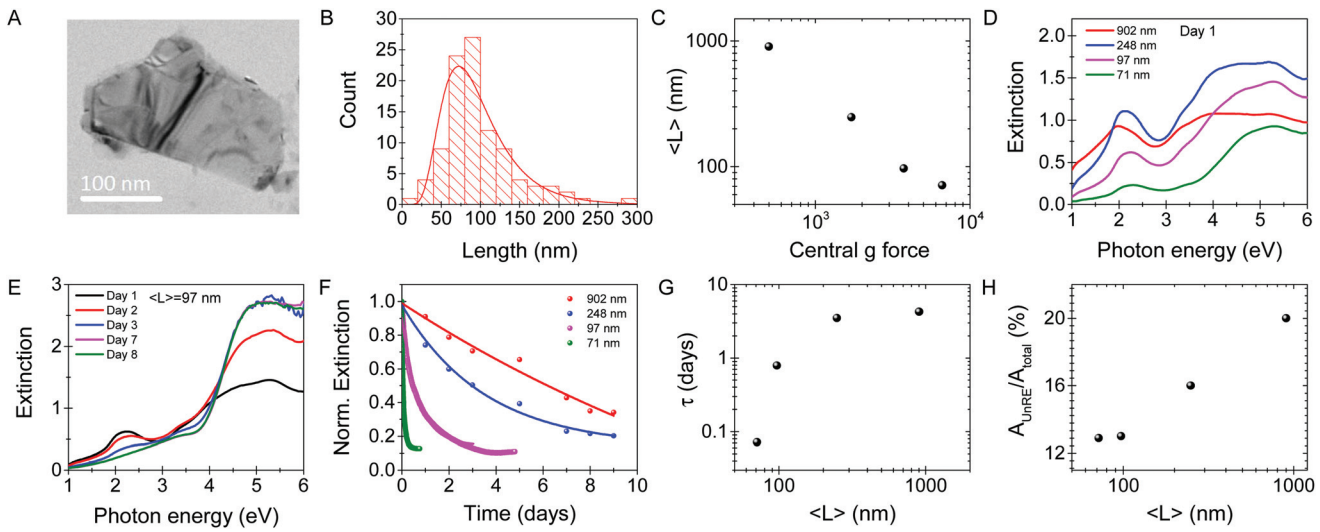

Fig. 2 Characterisation of size-selected TiS_2 nanosheets exfoliated in water–surfactant solutions. (A) Representative nanosheet from the fraction represented in the histogram; (B) histogram of the dispersion trapped between 3 and 5 krpm; (C) the mean nanosheet size measured for each fraction plotted *versus* the central *g*-force used during size selection. (D) Extinction spectra of size-selected fractions (labelled using the mean nanosheet length) measured immediately after preparation (fresh sample). (E) Evolution of extinction spectra for one fraction as a function of time after preparation. (F) Normalised extinction value, measured at 2.2 eV, plotted as a function of time after preparation for the fractions labelled using the mean nanosheet size. (G) Time constants obtained by fitting the data in E to single exponential decays plotted *versus* the mean nanosheet length. (H) Fraction of the unreacted material plotted *versus* mean nanosheet length.

One way to track the TiS_2 degradation is to study the evolution of extinction spectra over time. Shown in Fig. 2F are plots of the extinction at 2.2 eV normalized to its initial intensity plotted *versus* time after exfoliation for four different fractions (Fig. 2F). In each case, we find the extinction to fall steadily over time with the rate of decay increasing as the flake size decreases. For simplicity, we fit the experimental decays to an exponential function[37] (Fig. 2F) such that the normalized extinction is given by

$$\frac{\mathrm{Ext}(t)}{\mathrm{Ext}_0} = \frac{A_{\mathrm{UnRe}}}{A_{\mathrm{Total}}} + \left(1 - \frac{A_{\mathrm{UnRe}}}{A_{\mathrm{Total}}}\right) e^{-t/\tau} \quad (1)$$

where $A_{\mathrm{UnRe}}/A_{\mathrm{Total}}$ represents the fraction of TiS_2 that remains unoxidised after long times while τ represents the time constant of the oxidation process. Both the resultant time constants and $A_{\mathrm{UnRe}}/A_{\mathrm{Total}}$ values increase dramatically with nanosheet size ($\langle L \rangle$, Fig. 2G and H), indicating that small TiS_2 nanosheets are much more reactive compared to larger ones. This suggests that edge oxidation may be prevalent. We note that the timescales associated with this oxidation are short enough to make these materials unattractive candidates for applications unless somehow stabilized.

Exfoliation in a protecting solvent: cyclohexyl-pyrrolidone

Previously, cyclohexyl-pyrrolidone (CHP) has been proved to be an excellent solvent for the exfoliation of a range of 2D nanosheets.[37] In addition, it has been shown that highly unstable 2D materials such as black phosphorus can successfully be exfoliated without subsequent degradation in CHP.[37] Molecular dynamics simulations have suggested that CHP forms an ordered monolayer at the solvent–nanosheet interface,[38] providing a protective shell surrounding the nanosheets, shielding them from an attack by oxygen or water. With the aim of protecting TiS_2 nanosheets against oxidation, we repeat the exfoliation recipe described above but using CHP as the solvent instead of an aqueous SC solution. When this is done, the as-prepared stock dispersion does not exhibit the phase separation shown in Fig. 1A. Rather, a dark-purple dispersion that is indefinably stable is obtained.

To facilitate a fair comparison between TiS_2 degradation in CHP and in aqueous SC, a size-selection protocol similar to the one described above was performed, retaining the same centrifugation speeds while increasing the centrifugation time to 5 hours to partially compensate for the slower flake sedimentation due to the higher CHP viscosity.

As indicated above, the resultant size-selected fractions visually appear stable over time. TEM characterization showed well-defined nanosheets (Fig. 3A) with no sign of the nanoparticles shown in Fig. 1F. The TEM histograms reveal that the log-normal distribution of flake size is also present in the trapped TiS_2 dispersions in CHP (Fig. 3B). Again, we observed a well-defined evolution of $\langle L \rangle$ with the centrifugal speed yielding size-selected flakes (Fig. 3C).

The extinction spectra of the different dispersions show the same blue shift of the resonances as the flakes' size diminishes (Fig. 3D). In addition, pure absorption spectra (*i.e.* with scattering removed) of fresh CHP-exfoliated TiS_2 dispersions have been measured (see the ESI†). The absorption edge undergoes a monotonous blue shift as the flake size decreases, suggesting the opening of a bandgap in the monolayer regime.

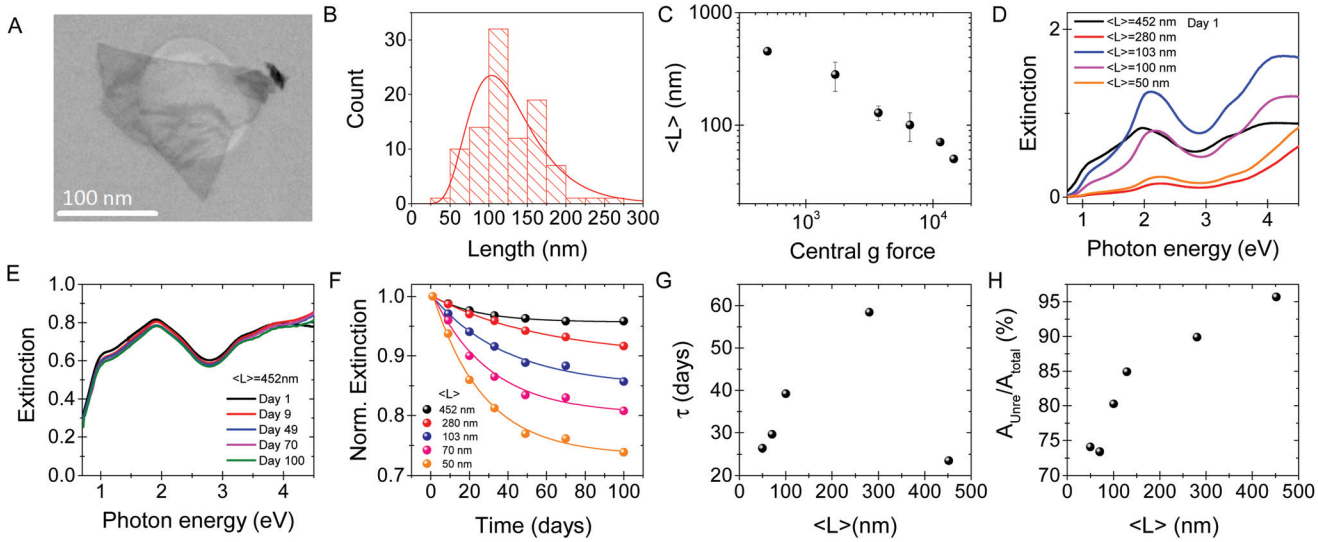

Fig. 3 Characterisation of size-selected TiS_2 nanosheets exfoliated in CHP solutions. (A) Representative nanosheet from the fraction represented in the histogram; (B) histogram of the dispersion trapped between 3 and 5 krpm; (C) the mean nanosheet size measured for each fraction plotted *versus* the central *g*-force used during size selection. (D) Extinction spectra of size-selected fractions (labelled using the mean nanosheet length) measured immediately after preparation (fresh sample). (E) Evolution of extinction spectra for one fraction as a function of time after preparation. (F) Normalised extinction value, measured at 2.2 eV, plotted as a function of time after preparation for the fractions labelled using the mean nanosheet size. (G) Time constants obtained by fitting the data in E to single exponential decays plotted *versus* the mean nanosheet length. (H) Fraction of the unreacted material plotted *versus* the mean nanosheet length.

Measuring the extinction spectrum of a given fraction over time (Fig. 3E) shows that TiS_2 flakes dispersed in CHP undergo minimal changes compared to the aqueous dispersion data shown in Fig. 2E and F, suggesting that TiS_2 oxidation is significantly reduced when CHP is used as solvent, as was previously observed for black phosphorus.[37] Plotting the normalized extinction at 2.2 eV *versus* time for each fraction (Fig. 3F) shows much slower and less complete degradation in CHP than in water. Using eqn (1) to fit the data in Fig. 3F, we can extract τ and A_{UnRe}/A_{Total} as before. The fit constants are plotted *versus* $\langle L \rangle$ in Fig. 3G and H. Both τ and A_{UnRe}/A_{Total} are much higher for the CHP-exfoliated nanosheets compared to nanosheets exfoliated in an aqueous environment as shown in Fig. 2. The degradation timescale was >20 days in all cases and monotonically increased with the flake lateral size, except for the dispersion with the largest flakes (Fig. 3G). This outlier is reproducible and may be an artifact of the size-selection procedure associated with poor long-term stability of very large flakes. As shown in Fig. 3H, the portion of unreacted material increases with nanosheet size, reaching values as high as 96%. These data confirm the hypothesis that oxidation is heavily suppressed in CHP. To support this statement, we have performed Raman measurements on all TiS_2-CHP dispersions with the previously observed degradation resonances not observable in samples as old as 110 days (the ESI†). Energy dispersive X-ray spectroscopy has been performed on fresh, one-month-old and 2-year-old sample TiS_2-CHP nanosheets; the dispersion was stable and no sign of oxidation was observed (the ESI†).

While the data given above suggest edge oxidation to be significant, it has previously been proposed that oxidation in TiS_2 starts from both edges and basal plane defects.[23,29] In the ESI,† we demonstrate a simple model to utilize the size dependent data in Fig. 2H to estimate the density of basal plane defects in TiS_2. Comparing the model to the data implies the defect concentration to be weakly nanosheet-size-dependent with typical values of $\sim 8 \times 10^{13}$ cm^{-2}. Similar values have been obtained for sulphur vacancies in other TMDs such as WS_2 and MoS_2 (3.5×10^{13} cm^{-2} sulphur vacancies in MoS_2 and 10^{14} cm^{-2} density of traps in WS_2).[35,39–41]

TiS_2 thin film degradation

TiS_2 nanosheets which had been exfoliated in both CHP and water/SC were transformed into thin films by vacuum filtration immediately after exfoliation and centrifugation. Raman spectra were collected at various times after film formation to investigate their stability (Fig. 4A and B). Immediately after film formation, although no oxide peaks were observed in the CHP-exfoliated film, oxide peaks broadly similar to those shown in Fig. 1C were observed in the aqueous-SC exfoliated sample. This is consistent with both the nanosheet instability observed in the water-based systems and the stability found in the CHP-exfoliated nanosheets. In the film prepared from water-exfoliated nanosheets, the oxide peaks increased in intensity over time, albeit very slowly (Fig. 4B). Such a slow oxidation indicates that while atmospheric water and oxygen are a problem, they do not present a catastrophic threat to dry, exfoliated TiS_2 over short timescales.

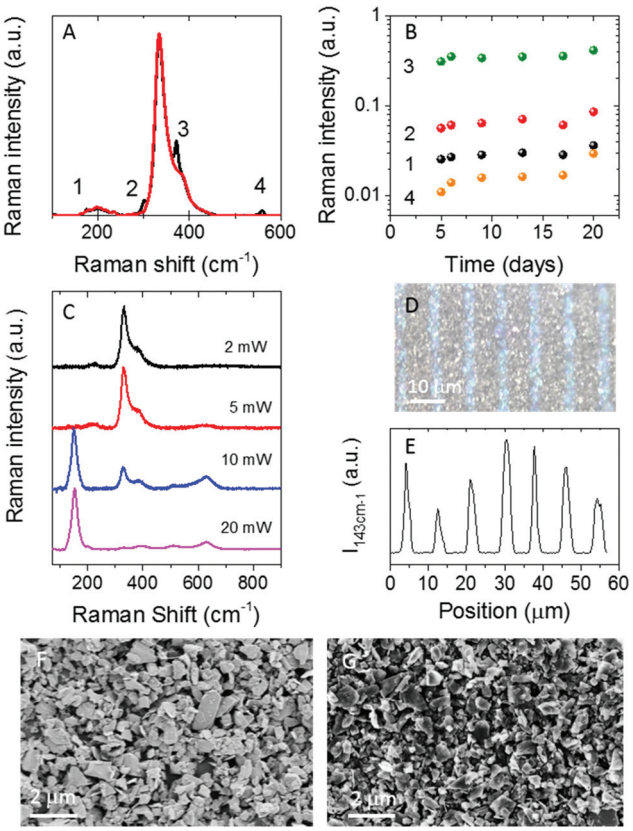

Fig. 4 (A) Raman spectra of TiS_2 films exfoliated in aqueous sodium cholate solution (black) and CHP (red) measured 30 days after deposition. (B) Time evolution of the oxide peaks in the sodium cholate solution sample (no oxide peaks were observed in the CHP sample at any stage). (C) Evolution of the Raman spectra with laser power, showing the photooxidation of the material from TiS_2 to TiO_2 (anatase). (D) Optical image of a TiS_2 film selectively photo-oxidised by laser scanning (20 mW). (E) Intensity of the 143 cm^{-1} resonance plotted as a function of position across the image in D. (F–G) SEM image of a deposited film before (F) and after (G) laser irradiation.

We found that no oxide peaks appeared in the films of CHP-exfoliated nanosheets even after 30 days (Fig. 4A). As CHP is a high boiling point solvent that binds strongly to the nanosheet surface, it can be hard to fully remove it from films. Thus, it is quite possible that some residual CHP present in the film coats the TiS_2 flakes protecting the film from degradation. Because the degradation of TiS_2 under ambient conditions is not measurable over timescales as long as 30 days after formation, this indicates that CHP-based exfoliation is a viable route to produce stable TiS_2 nanosheets and derive structures for applications.

Interestingly, TiS_2 films exfoliated in both aqueous SC solutions and CHP experience much more severe degradation when exposed to high light intensities. In order to avoid sample degradation during Raman measurements, we tested how the spectrum evolved on increasing the laser intensity.

Although no changes in the spectra were observed at powers below 0.2 mW (those we used to characterize the material), at higher intensities we observed a radical and rapid change in the spectra. In order to characterize this conversion, we irradiate the film for five minutes at different laser powers (2, 5, 10 and 20 mW) using a ~2 μm radius spot and measured the Raman spectra afterwards at low laser power (0.2 mW, Fig. 4C). The intensity of TiS_2 Raman resonances (~333 cm^{-1}) falls as the laser power increases, while the resonance at ~153 cm^{-1}, which can be attributed to anatase TiO_2, increases in intensity. This is consistent with a photoinduced transition from TiS_2 to anatase TiO_2.

The irradiated areas are recognizable due to a yellow-to-blue color change. Such a TiS_2 to anatase TiO_2 conversion is controllable and reproducible. Fig. 4D shows TiO_2 parallel lines patterned using a 20 mW laser power. If a Raman line scan is performed at low laser power perpendicular to the lines, the 153 cm^{-1} peak intensity can be plotted as a function of position, illustrating the spatial distribution of TiO_2 (Fig. 4E). SEM shows no significant morphological change in the nanosheets before and after irradiation (Fig. 4G and H), although the contrast variation is consistent with the change in the electronic structure. This implies that unlike the degradation that takes place in an aqueous environment, the photooxidized material retains the layered nature of TiS_2 and hence this may represent a route to produce TiO_2 nanosheets.

Applications of CHP-exfoliated TiS_2 nanosheets in battery electrodes

The ability to stabilise TiS_2 *via* exfoliation in CHP opens up opportunities for the use of this material in a range of applications. In particular, TiS_2 shows promise for lithium storage applications, displaying a reasonably high theoretical specific capacity (~960 mA h g^{-1}) and low volume change during the discharge/charge process.[42–44] In addition, its layered structure allows fast diffusion of Li ions; among all the transition metal dichalcogenides, TiS_2 has the lowest density, making it a promising candidate for high-specific-energy rechargeable LIBs.

As long ago as 1976, bulk TiS_2 was used to produce the first Li/TiS_2 battery, which showed a very high capacity and long cycle life.[18] Unfortunately, because of lithium dendrite formation in liquid electrolytes, Li/TiS_2 cells are unsafe, which limits the application of this material.[45] However, recently, researchers have re-examined TiS_2 as a lithium storage material.[46–52] Zhang *et al.*[53] found that anodes fabricated from bulk TiS_2 displayed a high initial capacity of 936 mA h g^{-1}, which subsequently decayed rapidly to less than 400 mA h g^{-1} over the first 20 cycles when tested with a cut-off potential of 0.05–3.0 V. Conversely, cells tested with a cut-off potential of 1.4–3.0 V displayed very stable cycle-ability, albeit at capacities below 200 mA h g^{-1}.

Such a severe capacity-fade has previously been observed in lithium ion battery electrodes fabricated from bulk MoS_2. However, it was found that this could be successfully resolved using exfoliated MoS_2 nanosheets rather than bulk layered material.[54] This would imply that using liquid-exfoliated TiS_2 nanosheets could yield stable LiB anodes. A number of papers have used growth[55] or chemical synthesis[56] to prepare TiS_2 nanosheets for battery applications. However, to our knowledge, liquid exfoliation methods have not been used to produce TiS_2 for such applications, probably due to the stability issues outlined above. This is a considerable gap in the literature as the inherent scalability of liquid exfoliation techniques makes them attractive candidates for low cost material production.[57,58] To address this, here we will demonstrate the use of CHP-exfoliated TiS_2 nanosheets to prepare anodes for lithium ion batteries.

Films composed solely of nanosheets tend to have low electrical conductivity and usually display poor mechanical properties.[59] Recently, we have shown that both of these deficiencies can be addressed by adding carbon nanotubes to the nanosheets (without the need for additional binders) to form a nano : nano composite.[59] When such nano : nano composites are used as battery electrodes, they tend to show excellent performance,[13] displaying specific capacities (normalised to active mass) that approach the theoretical value.[60] In this work, we prepared TiS_2-based electrodes by adding single wall nanotubes (SWNT) to the TiS_2/CHP dispersion such that SWNT made up 20% of the solid mass. These dispersions were then transformed into electrodes as described in the Materials & methods section. Single walled nanotubes tend to have Li storage capacities of ~80–170 mA h g^{-1}.[61] As such, we would not expect the 20 wt% nanotube fraction to contribute more than ~15–30 mA h g^{-1} to the overall electrode capacity. Thus we believe that the measured capacity will be dominated by the contribution of TiS_2.

We first performed cyclic voltammetry (CV) to characterise the electrochemical reactions occurring in our TiS_2-based anodes (with mass loadings of 0.6 mg cm^{-2} TiS_2 and 0.15 mg cm^{-2} SWNT). A subset of the CV curves associated with the first fifty lithiation–delithiation cycles are shown in Fig. 5A–G. The potential is swept from the open circuit voltage to 0.05 V followed by a further sweep between 0.05 and 3.0 V at a scan rate of 0.1 mV s^{-1}. For the 1st cycle, the reduction peaks are at 1.6–2.5 V, corresponding to the intercalation reaction of the TiS_2 electrode ($TiS_2 + xLi^+ + xe^- \rightarrow Li_xTiS_2$ ($0 < x < 1$)), with the corresponding oxidation peaks appearing at 1.8–2.5 V. These peaks continue to be present when the electrode is cycled in the potential range 1.4–3 V but disappear when cycled between 0.05 and 3 V after only 2 cycles. This is consistent with the data of Zhang *et al.*[53] and indicates the rapid electrochemical conversion of TiS_2 into another species (see below).

The presence of a conversion reaction is indicated by reduction peaks at 0.3–0.5 V ($LiTiS_2 + 3Li^+ + 3e^- \rightarrow 2Li_2S + Ti$) and the corresponding oxidation peaks are at 0.5–1.6 V.[53] These peaks may also be associated with the formation of the SEI (solid–electrolyte interface) layer, and have been significantly attenuated and broadened by the 5th cycle.

However, the most interesting part is the oxidation peaks at 2.5–2.8 V after 5 cycles in our study, which were not observed in Zhang's study.[53] These peaks are attributed to the conver-

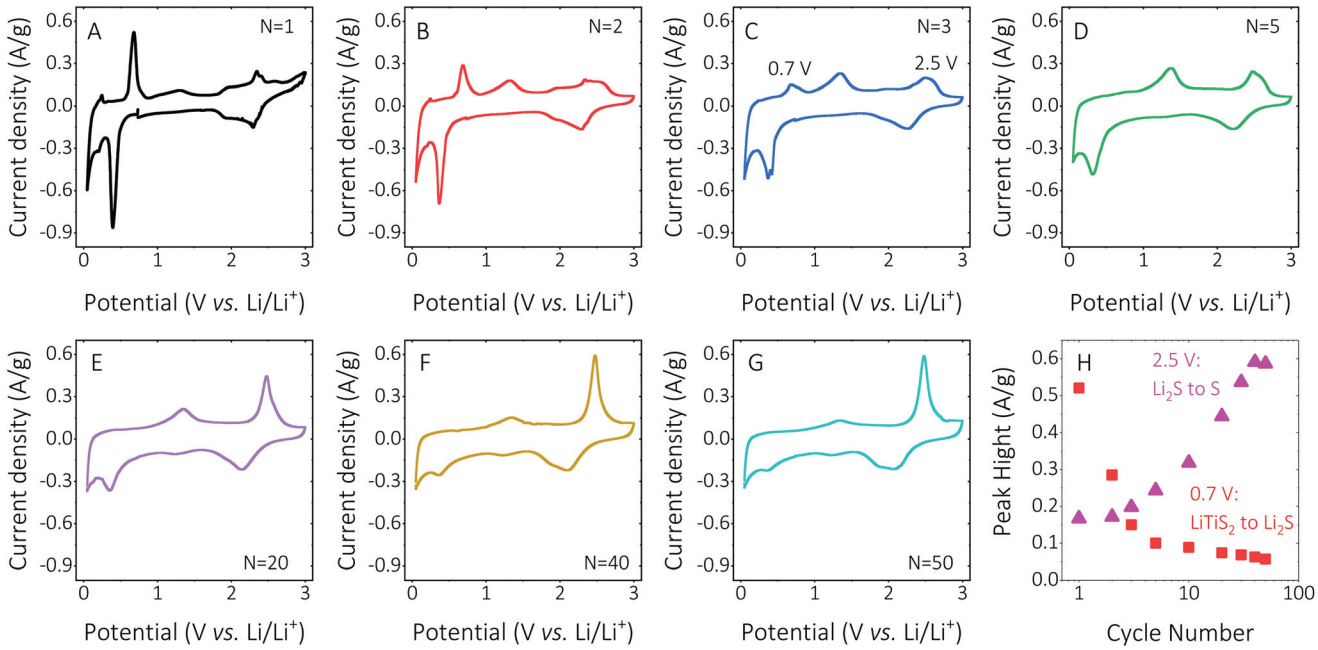

Fig. 5 (A–G) Cyclic voltammograms measured on a TiS_2/SWCNT (20 wt%) electrode at a scan rate of 0.1 mV s^{-1} in the voltage range of 0.05–3.0 V *vs.* Li/Li^+ for a wide range of cycle numbers. (H) Heights of the oxidation peaks at 0.7 V (red square) and 2.5 V (magenta triangle) plotted *versus* cycle number.

sion of lithium sulfides into sulfur ($8Li_2S \rightarrow 16Li + S_8$), with the corresponding reduction peaks appearing at 1.8–1.9 V (ref. 62), and are evidence of phase transitions from TiS_2 to Li_2S in our exfoliated TiS_2 nanosheets. Similar peaks have been observed in other battery studies based on other TMDs such as MoS_2.[13,63] Furthermore, CV measurements after 50 cycles (Fig. 5G) show the strongest oxidation peaks at 2.5–2.8 V, with reduction peaks at 1.8–2.2 V, while the oxidation peak at 1.4 V was very weak, which indicated that most of the phase transitions from TiS_2 to Li_2S had completed.

From Zhang's study,[53] the intercalation reaction peaks of the TiS_2 electrode ($TiS_2 + xLi^+ + xe^- \rightarrow Li_xTiS_2$ ($0 < x < 1$) disappeared after 2 cycles once the cut-off voltage had decreased to 0.05 V. Thereafter, the capacity decreased rapidly (a reduction of about 200 mA h g^{-1}). Including the partially reversible conversion reaction ($LiTiS_2 + 3Li^+ + 3e^- \rightarrow 2Li_2S +$ Ti), the normal capacity was below 500 mA h g^{-1}.[53,64,65] However, in our study, the conversion of TiS_2 to Li_2S appeared to proceed to completion, meaning that the predominant reactions were associated with a cycling between Li_2S and S with a very high reversibility. As a result, the capacity was much more stable than in other studies.[53,64,65]

We can summarise these results by plotting the heights of the oxidation peaks at 0.7 V ($LiTiS_2$ to Li_2S) and 2.5 V (Li_2S to S) against cycle number as shown in Fig. 5H. Once the intercalation reaction has decayed rapidly after a few cycles, the $LiTiS_2$-to-Li_2S conversion (0.7 V) becomes the predominant reaction. However, the peaks associated with this reaction die away almost completely after 5–10 cycles, indicating that the conversion to Li_2S goes largely to completion. Over the same range of cycles the peak at 2.5 V associated with the reversible Li_2S-to-S conversion grows steadily, saturating after 30–40 cycles, indicating that this has become the dominant reaction.

We then measured galvanostatic charge–discharge curves and capacity *versus* cycle number data as shown in Fig. 6A and B. We found that TiS_2 nanosheet electrodes exhibited good lithium storage capability. Measuring at a specific current of 1.0 A g^{-1} for 100 cycles, the discharge and charge capacities were initially 826 and 803 mA h g^{-1} (with 97.2% CE). After 100 cycles the values were 843 and 838 mA h g^{-1} (with 99.5% CE). We also tested the rate performance of our electrodes as shown in Fig. 6C and D. These electrodes exhibited an initial performance of 1055 mA h g^{-1} for discharge and 921 mA h g^{-1} for charge at 0.1 A g^{-1}. At 0.2 A g^{-1}; the capacity is 912 mA h g^{-1} for discharge and 938 mA h g^{-1} for charge, with an increase to 915 and 954 mA h g^{-1} after 10 cycles. These values are very close to the theoretical value of 960 mA h g^{-1}.[53] Furthermore, the composite electrode is capable of fast charge and discharge. When the specific currents were increased to 0.5, 1, 2 and 4 A g^{-1}, specific charge capacities of 890, 849, 752 and 592 mA h g^{-1}, respectively, are reversibly delivered. On returning the current rate to 0.1 A g^{-1}, the specific discharge and charge capacities increased to 1025 and 1088 mA h g^{-1}, respectively. The capacity is a little higher than the theoretical capacity; this may be attributed to the pseudo capacity related to the surface area.

As described above, we have found that TiS_2/SWNT (20 wt%) composite electrodes can deliver stable capacities of up to ~1000 mA h g^{-1} at low charge/discharge rates. As mentioned above, we expect no more than 15–30 mA h h^{-1} to come

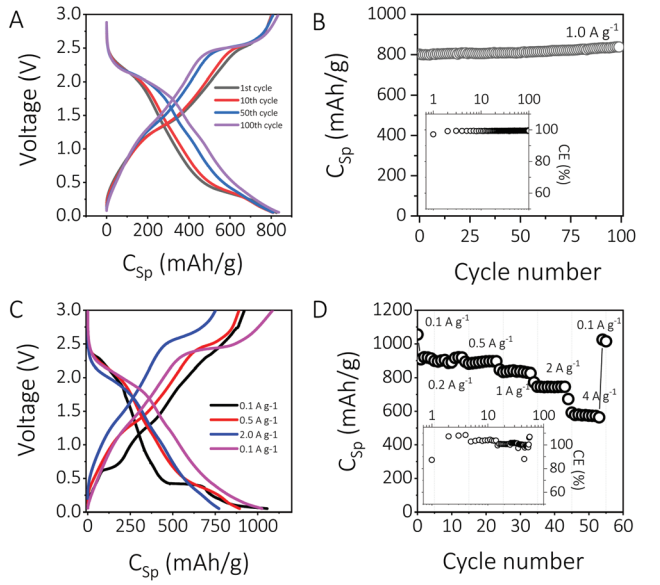

Fig. 6 Performance of composites of TiS_2 nanosheets/SWCNT (20 wt%) used as lithium ion battery anodes. (A) Galvanostatic charge–discharge curves for different numbers of cycles (1.0 A g^{-1}). (B) Cycling (charging) capacity *versus* cycle number measured at 1.0 A g^{-1} with the Coulomb efficiency shown in the inset. (C) Galvanostatic charge–discharge curves measured at different current rates. (D) The capacity as a function of current rate with the Coulomb efficiency shown in the inset.

from lithium storage associated with the nanotubes. This means that the storage associated with TiS_2 is very close to the theoretical capacity (960 mA h g^{-1}). These capacities are significantly higher than those previously reported for TiS_2-based lithium battery electrodes which achieved stable, reversible capacities of no more than 670 mA h g^{-1}.[53,64,65] Although capacities as high as 936 mA h g^{-1} (ref. 53) have been reported for bulk TiS_2, such electrodes were not stable with cycling. All the battery data given above indicate that combining our exfoliated TiS_2 nanosheets with CNTs yields electrodes with high capacity, good rate performance and excellent cycle-ability. The outstanding lithium storage performance of the TiS_2/CNTs nanocomposite may be attributed to a combination of the high intrinsic capacity of TiS_2 and fast Li ion diffusion associated with the open 2D structure, as well as the direct effects of the CNT network,[13,66] which not only improves conductivity and so facilitates fast charge delivery, but also enhances the mechanical stability of the electrodes on cycling.

Conclusions

In summary, we have found that while TiS_2 can be exfoliated by sonication in aqueous surfactant dispersions, the resultant nanosheets were chemically unstable, almost completely oxidizing into titanium oxide within days. However, when the exfoliation was performed in the amide solvent cyclohexyl-pyrrolidone (CHP), the nanosheets were much more stable. After solvent exfoliation, although some oxidation may have occurred, in general over 75% of the exfoliated TiS_2 was still present in the dispersion 100 days after exfoliation. We note that for both aqueous exfoliation and solvent exfoliation, small nanosheets tend to be more unstable, suggesting that oxidation may predominantly occur at nanosheet edges. Importantly, films prepared from CHP-exfoliated nanosheets did not exhibit signs of subsequent oxidation when stored under ambient conditions for at least 30 days, possibly due to the stabilizing action of residual solvent. This stabilizing effect of CHP makes it feasible to use TiS_2 nanosheets in applications. For example, nano : nano composite films of TiS_2 mixed with carbon nanotubes have been used to produce lithium ion battery anodes. These anodes displayed specific capacity, rate performance and cycle-ability that were considerably better than those of any previous reports.

Materials & methods

Pristine powder TiS_2 was purchased from Sigma-Aldrich (SKU 333492). The following solvents have been used: deionized water type I (18 MΩ cm^{-1}) and cyclohexyl-pyrrolidone (Sigma-Aldrich; SKU 232254). SEM and Raman investigations (see the ESI†) showed the starting material to be consistent with layered TiS_2 powder.

Aqueous surfactant dispersions

TiS_2 powder was mixed with 14 mL water and sodium cholate (the starting concentrations were C_{SC} = 2 g L^{-1} and C_{TiS_2} = 20 g L^{-1}) and sonicated for one hour using a tapered tip (VibraCell CVX; 750 W), and pulsed (6 s on and 2 s off) at 30% power under ice bath cooling. This stock dispersion exhibited the phase separation as shown in Fig. 1.

To study the size dependent TiS_2 degradation in aqueous surfactant dispersions (Fig. 2), a similar stock dispersion was centrifuged at 1000 rpm for 90 minutes, the sediment was discarded and the supernatant was then centrifuged again at 3000 rpm. The second sediment was redispersed in 14 mL of water and SC (C_{SC} = 2 g L^{-1}) and the supernatant was centrifuged at 5000 rpm. This procedure was repeated at 7000, 9000 and 12 000 rpm.

CHP dispersion

TiS_2 powder was added to 14 mL CHP (at a starting concentration of C_{TiS_2} = 20 g L^{-1}) and sonicated for one hour using a tapered tip (VibraCell CVX; 750 W), and pulsed (6 s on and 2 s off) at 30% power under ice bath cooling.

To study the size dependent TiS_2 degradation in CHP (Fig. 3), this stock dispersion was centrifuged at 1000 rpm for 5 hours, the sediment was discarded and the supernatant was then centrifuged again at 3000 rpm. The second sediment was redispersed in 14 mL CHP and the supernatant was centrifuged at 5000 rpm. This procedure was repeated at 7000, 9000 and 12 000 rpm.

Filtered films for Raman measurements

10 mL of a TiS_2 dispersion trapped between 1000 and 3000 rpm were sprayed on a microscope glass slide following a previously reported protocol.[67] The dispersion concentration was set to 1.5 g L^{-1} prior to spraying. The sample was kept under vacuum for 12 hours.

Energy dispersive X-ray spectroscopy

EDX was performed using a JEOL 2100 LaB TEM with an 80 mm^2 XMAX EDX detector. In contrast to the low resolution imaging where a five specimen holder is used, here a single specimen holder is used with a tilt of 20° with respect to the beam to reduce any interference between the holder and the nanosheets. Besides this, all EDX spectra were taken with the centre of each grid to reduce interference from the copper supports. For each sample the EDX spectra of fifty nanosheets were measured and averaged to yield the elemental ratios.

Battery preparation

TiS_2 dispersions trapped between 1000 and 3000 rpm were mixed with single walled carbon nanotubes (SCNTs). These dispersions were vacuum-filtered using porous cellulose filter membranes (MF-Millipore membrane mixed cellulose esters, hydrophilic, 0.025 μm, 47 mm) to give thin films with 20 wt% SWCNTs. 0.1 mg mL^{-1} dispersions of SWCNT were prepared by dispersing 10 mg of P3-SWCNT in 100 mL of IPA for one hour in a Fisherbrand Ultrasonic Dismembrator (30 W, 40% amplitude). The mass loading of these films was controlled by the volume of dispersion filtered.

The resulting films (diameter, 36 mm) were cut to the desired dimensions for electrochemical testing and then transferred to Cu foils. For transferring, IPA was used to adhere the electrode side of the film to the substrate; thus the cellulose filter membrane was exposed to the air. Then, the cellulose filter membrane was removed by treatment with acetone vapor for 30 min. The mass loading of TiS_2 is 0.6 mg cm^{-2} for rate capability measurements and cycling performance measurements.

Li-ion storage

For the electrochemical measurement, metallic lithium foils (diameter: 14 mm; MTI Corp.) were used as the negative electrode. The electrolyte used was 1 M $LiPF_6$ in a 1 : 1 (volume ratio) mixture of ethylene carbonate (EC) and dimethyl carbonate (DMC) with 10 wt% Fluoroethylene Carbonate (FEC) as an additive. A Celgard 2320 instrument was used as the separator. The cells were assembled in a glove box filled with highly pure argon gas (O_2 and H_2O levels <0.1 ppm), and the electrochemical properties of the electrodes were measured within a voltage range of 3.0–0.05 V using the constant current (CC) mode on an automatic battery tester (VMP 3, BioLogic). For rate capability measurements, cells were running at different current rates of 0.1 A g^{-1}, 0.2 A g^{-1}, 0.5 A g^{-1}, 1 A g^{-1}, 2 A g^{-1}, and 4 A g^{-1} and then went back to 0.1 A g^{-1}. There are only 4 cycles at 0.1 A g^{-1} for activation and 2 cycles for going back, and there are 10 cycles for other steps at different current rates. For cycling capability tests, the cells were performed at 1.0 A g^{-1} for 100 cycles. Cyclic voltammetry of the cells was carried out using a galvanostat–potentiostat between 0.05 and 3.0 V at a scanning rate of 0.1 mV s^{-1} for 50 cycles.

Optical spectroscopy

A PerkinElmer Lambda 1050 spectrometer was used to measure the extinction spectra. The samples were diluted to a suitable optical density and measured using a quartz cuvette with an optical path length of 2 mm.

Raman spectroscopy

Raman spectroscopy was performed on the devices prior to IL deposition using a Horiba Jobin Yvon LabRAM HR800 instrument with a 532 nm excitation laser in air under ambient conditions. The Raman emission was collected using a 100× objective lens (N.A. = 0.8) and dispersed by a 600 line per mm grating to obtain a resolution of ~1 cm^{-1}. 1% of the laser power (~0.2 mW) was used for the Raman measurements in a ~2 μm radius spot. For TiS_2 photooxidation 10, 25, 50 and 100% laser powers were used (2, 5, 10, and 20 mW).

TEM characterization

Bright-field transmission electron microscopy (TEM) was performed using a JOEL 2100 instrument operated at 200 kV. Samples were diluted to a low concentration and drop-cast on a continuous carbon film TEM grid purchased from Agar Scientific. The TEM grid was placed on a filter membrane to wick away excess solvent and dried overnight at room temperature in a vacuum oven. Statistical analysis was performed on the nanosheet dimensions by measuring the longest axis and defining it as the nanosheet length.

Conflicts of interest

There are no conflicts to declare.

Acknowledgements

This work was primarily funded by European Union Seventh Framework Program under grant agreements 604391 and 785219 Graphene Flagship and the Science Foundation Ireland (SFI) funded centre AMBER (SFI/12/RC/2278). We also acknowledge support from the ERC Advanced Grant FUTUREPRINT.

References

1 J. Yang, J. X. Zhu, J. S. Xu, C. Zhang and T. Liu, *ACS Appl. Mater. Interfaces*, 2017, **9**, 44550–44559.
2 K. Wang, J. Yang, J. X. Zhu, L. Li, Y. Liu, C. Zhang and T. X. Liu, *J. Mater. Chem. A*, 2017, **5**, 11236–11245.

3 K. Wang, L. Li, Y. Liu, C. Zhang and T. Liu, *Adv. Mater. Interfaces*, 2016, **3**, 1600665.
4 F. Bonaccorso, L. Colombo, G. H. Yu, M. Stoller, V. Tozzini, A. C. Ferrari, R. S. Ruoff and V. Pellegrini, *Science*, 2015, **347**, 1246501.
5 A. E. D. Castillo, V. Pellegrini, H. Y. Sun, J. Buha, D. A. Dinh, E. Lago, A. Ansaldo, A. Capasso, L. Manna and F. Bonaccorso, *Chem. Mater.*, 2018, **30**, 506–516.
6 C. Sole, N. E. Drewett, F. Liu, A. M. Abdelkader, I. A. Kinloch and L. J. Hardwick, *J. Electroanal. Chem.*, 2015, **753**, 35–41.
7 H. Y. Sun, D. Hanlon, D. A. Dinh, J. B. Boland, A. E. D. Castillo, C. Di Giovanni, A. Ansaldo, V. Pellegrini, J. N. Coleman and F. Bonaccorso, *2D Mater.*, 2018, **5**, 015024.
8 Y. Y. Wang, J. H. Zhou, J. H. Wu, F. J. Chen, P. R. Li, N. Han, W. J. Huang, Y. P. Liu, H. L. Ye, F. P. Zhao and Y. G. Li, *J. Mater. Chem. A*, 2017, **5**, 25618–25624.
9 F. X. Wu, J. T. Lee, E. B. Zhao, B. Zhang and G. Yushin, *ACS Nano*, 2016, **10**, 1333–1340.
10 K. S. Novoselov, A. K. Geim, S. V. Morozov, D. Jiang, Y. Zhang, S. V. Dubonos, I. V. G. Grigorieva and A. A. Firsov, *Science*, 2004, **306**, 666–669.
11 A. K. GEIM and K. S. NOVOSELOV, *Nat. Mater.*, 2007, **6**, 183–191.
12 S. Manzeli, D. Ovchinnikov, D. Pasquier, O. V. Yazyev and A. Kis, *Nat. Rev. Mater.*, 2017, **2**, 17033.
13 Y. P. Liu, X. Y. He, D. Hanlon, A. Harvey, U. Khan, Y. G. Li and J. N. Coleman, *ACS Nano*, 2016, **10**, 5980–5990.
14 D. Vella, D. Ovchinnikov, N. Martino, V. Vega-Mayoral, D. Dumcenco, Y.-C. Kung, M.-R. Antognazza, A. Kis, G. Lanzani, D. Mihailovic and C. Gadermaier, *2D Mater.*, 2017, **4**, 021005.
15 D. Xiang, T. Liu, J. L. Xu, J. Y. Tan, Z. H. Hu, B. Lei, Y. Zheng, J. Wu, A. H. C. Neto, L. Liu and W. Chen, *Nat. Commun.*, 2018, **9**, 2966.
16 S. J. Varma, J. Kumar, K. Layne, J. Wu, C. Liang, Y. Nakanishi, A. Aliyan, W. Yang, P. M. Ajayan and J. Thomas, *Adv. Opt. Mater.*, 2017, **5**, 1700713.
17 Y. Zhou, J. Y. Wan, Q. Li, L. Chen, J. Y. Zhou, H. A. Wang, D. R. He, X. R. Li, Y. C. Yang and H. H. Huang, *ACS Appl. Mater. Interfaces*, 2017, **9**, 42430–42437.
18 M. S. Whittingham, *Science*, 1976, **192**, 1126–1127.
19 J. Caja, R. B. Kaner and A. G. MacDiarmid, *J. Electrochem. Soc.*, 1984, **131**, 2744.
20 G. L. Holleck and J. R. Driscoll, *Electrochim. Acta*, 1977, **22**, 647–655.
21 Z. W. Seh, Y. Sun, Q. Zhang and Y. Cui, *Chem. Soc. Rev.*, 2016, **45**, 5605–5634.
22 K. H. Park, J. Choi, H. J. Kim, D. H. Oh, J. R. Ahn and S. U. Son, *Small*, 2008, **4**, 945–950.
23 E. Long, S. O'Brien, E. A. Lewis, E. Prestat, C. Downing, C. S. Cucinotta, S. Sanvito, S. J. Haigh and V. Nicolosi, *npj 2D Mater. Appl.*, 2017, **1**, 22.
24 C. Xu, P. A. Brown and K. L. Shuford, *RSC Adv.*, 2015, **5**, 83876–83879.
25 K. Dolui and S. Sanvito, *EPL*, 2016, **115**, 47001.
26 P. Chen, Y. H. Chan, X. Y. Fang, Y. Zhang, M. Y. Chou, S. K. Mo, Z. Hussain, A. V. Fedorov and T. C. Chiang, *Nat. Commun.*, 2015, **6**, 8943.
27 A. Samad, A. Shafique and Y. H. Shin, *Nanotechnology*, 2017, **28**, 175401.
28 L. H. Yuwen, H. Yu, X. R. Yang, J. J. Zhou, Q. Zhang, Y. Q. Zhang, Z. M. Luo, S. Su and L. H. Wang, *Chem. Commun.*, 2016, **52**, 529–532.
29 C. S. Cucinotta, K. Dolui, H. Pettersson, Q. M. Ramasse, E. Long, S. E. O'Brian, V. Nicolosi and S. Sanvito, *J. Phys. Chem. C*, 2015, **119**, 15707–15715.
30 N. N. Greenwood and A. Earnshaw, *Chemistry of the Elements*, 2nd edn, 1997.
31 S. Wild, V. Lloret, V. Vega-Mayoral, D. Vella, E. Nuin, M. Siebert, M. Koleśnik-Gray, M. Löffler, K. J. J. Mayrhofer, C. Gadermaier, V. Krstić, F. Hauke, G. Abellán and A. Hirsch, *RSC Adv.*, 2019, **9**, 3570–3576.
32 P. C. Klipstein, A. G. Bagnall, W. Y. Liang, E. A. Marseglia and R. H. Friend, *J. Phys. C: Solid State Phys.*, 1981, **14**, 4067–4081.
33 G. Meinhold, B. Anders, D. Kostopoulos and R. Thomas, *Sediment. Geol.*, 2008, **203**, 8–11.
34 S. V. Ovsyannikov, X. Wu, V. V. Shchennikov, A. E. Karkin, N. Dubrovinskaia, G. Garbarino and L. Dubrovinsky, *J. Phys.: Condens. Matter*, 2010, **22**, 375402.
35 C. Backes, B. M. Szydłowska, A. Harvey, S. Yuan, V. Vega-Mayoral, B. R. Davies, P.-l. Zhao, D. Hanlon, E. J. G. Santos, M. I. Katsnelson, W. J. Blau, C. Gadermaier and J. N. Coleman, *ACS Nano*, 2016, **10**, 1589–1601.
36 C. Backes, R. J. Smith, N. McEvoy, N. C. Berner, D. McCloskey, H. C. Nerl, A. O'Neill, P. J. King, T. Higgins, D. Hanlon, N. Scheuschner, J. Maultzsch, L. Houben, G. S. Duesberg, J. F. Donegan, V. Nicolosi and J. N. Coleman, *Nat. Commun.*, 2014, **5**, 4576.
37 D. Hanlon, C. Backes, E. Doherty, C. S. Cucinotta, N. C. Berner, C. Boland, K. Lee, A. Harvey, P. Lynch, Z. Gholamvand, S. Zhang, K. Wang, G. Moynihan, A. Pokle, Q. M. Ramasse, N. McEvoy, W. J. Blau, J. Wang, G. Abellan, F. Hauke, A. Hirsch, S. Sanvito, D. D. O'Regan, G. S. Duesberg, V. Nicolosi and J. N. Coleman, *Nat. Commun.*, 2015, **6**, 8563.
38 V. Sresht, A. A. H. Pádua and B. Daniel, *ACS Nano*, 2015, **9**, 8255–8268.
39 V. Vega-Mayoral, T. Borzda, D. Vella, M. Prijatelj, E. A. A. Pogna, C. Backes, J. N. Coleman, G. Cerullo, D. Mihailovic and C. Gadermaier, *2D Mater.*, 2017, **5**, 015011.
40 J. Hong, Z. Hu, M. Probert, K. Li, D. Lv, X. Yang, L. Gu, N. Mao, Q. Feng, L. Xie, J. Zhang, D. Wu, Z. Zhang, C. Jin, W. Ji, X. Zhang, J. Yuan and Z. Zhang, *Nat. Commun.*, 2015, **6**, 6293.
41 V. Vega-Mayoral, D. Vella, T. Borzda, M. Prijatelj, I. Tempra, E. A. A. Pogna, S. Dal Conte, P. Topolovsek, N. Vujicic, G. Cerullo, D. Mihailovic and C. Gadermaier, *Nanoscale*, 2016, **8**, 5428–5434.

42 C. Tan, X. Cao, X. J. Wu, Q. He, J. Yang, X. Zhang, J. Chen, W. Zhao, S. Han, G. H. Nam, M. Sindoro and H. Zhang, *Chem. Rev.*, 2017, **117**, 6225–6331.
43 Y. Zhang, Q. Zhou, J. Zhu, Q. Yan, S. X. Dou and W. Sun, *Adv. Funct. Mater.*, 2017, **27**, 1702317.
44 T. Wang, S. Chen, H. Pang, H. Xue and Y. Yu, *Adv. Sci.*, 2017, **4**, 1600289.
45 J.-M. Tarascon and M. Armand, *Nature*, 2001, **414**, 359–367.
46 Y. Liu, G. Zhou, K. Liu and Y. Cui, *Acc. Chem. Res.*, 2017, **50**, 2895–2905.
47 D. Lin, Y. Liu and Y. Cui, *Nat. Nanotechnol.*, 2017, **12**, 194–206.
48 X. Liang, Q. Pang, I. R. Kochetkov, M. S. Sempere, H. Huang, X. Sun and L. F. Nazar, *Nat. Energy*, 2017, **2**, 17119.
49 X. Zang, C. Shen, E. Kao, R. Warren, R. Zhang, K. S. Teh, J. Zhong, M. Wei, B. Li, Y. Chu, M. Sanghadasa, A. Schwartzberg and L. Lin, *Adv. Mater.*, 2017, **30**, 1704754.
50 J. M. Whiteley, S. Hafner, S. S. Han, S. C. Kim, V.-D. Le, C. Ban, Y. H. Kim, K. H. Oh and S.-H. Lee, *J. Mater. Chem. A*, 2017, **5**, 15661–15668.
51 A. Chaturvedi, P. Hu, V. Aravindan, C. Kloc and S. Madhavi, *J. Mater. Chem. A*, 2017, **5**, 9177–8181.
52 D. Y. Oh, Y. E. Choi, D. H. Kim, Y.-G. Lee, B.-S. Kim, J. Park, H. Sohn and Y. S. Jung, *J. Mater. Chem. A*, 2016, **4**, 10329–10335.
53 L. Zhang, D. Sun, J. Kang, H.-T. Wang, S.-H. Hsieh, W.-F. Pong, H. A. Bechtel, J. Feng, L.-W. Wang, L.-J. Cairns and J. Guo, *Nano Lett.*, 2018, **18**, 4506–4515.
54 Y. D. Liu, L. Ren, X. Qi, L. W. Yang, J. Li, Y. Wang and J. X. Zhong, *J. Energy Chem.*, 2014, **23**, 207–212.
55 A. Chaturvedi, E. Edison, N. Arun, P. Hu, C. Kloc, V. Aravindan and S. Madhavi, *ChemistrySelect*, 2018, **3**, 524–528.
56 Y. P. Liu, H. T. Wang, L. Cheng, N. Han, F. P. Zhao, P. R. Li, C. H. Jin and Y. G. Li, *Nano Energy*, 2016, **20**, 168–175.
57 A. E. Del Rio Castillo, V. Pellegrini, A. Ansaldo, F. Ricciardella, H. Sun, L. Marasco, J. Buha, Z. Dang, L. Gagliani, E. Lago, N. Curreli, S. Gentiluomo, F. Palazon, M. Prato, R. Oropesa-Nuñez, P. S. Toth, E. Mantero, M. Crugliano, A. Gamucci, A. Tomadin, M. Polini and F. Bonaccorso, *Mater. Horiz.*, 2018, **5**, 890–904.
58 K. R. Paton, E. Varrla, C. Backes, R. J. Smith, U. Khan, A. O'Neill, C. Boland, M. Lotya, O. M. Istrate, P. King, T. Higgins, S. Barwich, P. May, P. Puczkarski, I. Ahmed, M. Moebius, H. Pettersson, E. Long, J. Coelho, S. E. O'Brien, E. K. McGuire, B. M. Sanchez, G. S. Duesberg, N. McEvoy, T. J. Pennycook, C. Downing, A. Crossley, V. Nicolosi and J. N. Coleman, *Nat. Mater.*, 2014, **13**, 624–630.
59 C. Gabbett, C. S. Boland, A. Harvey, V. Vega-Mayoral, R. J. Young and J. N. Coleman, *Chem. Mater.*, 2018, **30**, 5245–5255.
60 C. F. Zhang, S. H. Park, O. Ronan, A. Harvey, A. Seral-Ascaso, Z. F. Lin, N. McEvoy, C. S. Boland, N. C. Berner, G. S. Duesberg, P. Rozier, J. N. Coleman and V. Nicolosi, *Small*, 2017, **13**, 1701677.
61 S. B. Yang, J. P. Huo, H. H. Song and X. H. Chen, *Electrochim. Acta*, 2008, **53**, 2238–2244.
62 L. Wang, Y. G. Wang and Y. Y. Xia, *Energy Environ. Sci.*, 2015, **8**, 1551–1558.
63 T. Stephenson, Z. Li, B. Olsen and D. Mitlin, *Energy Environ. Sci.*, 2014, **7**, 209–231.
64 S.-Y. Chen, Z.-X. Wang, X.-P. Fang, H.-L. Zhao, X.-J. Liu and L.-Q. Chen, *Acta Phys.-Chim. Sin.*, 2011, **27**, 97–102.
65 B. Kartick, S. K. Srivastava and S. Mahanty, *J. Nanopart. Res.*, 2013, **15**, 1950.
66 Z. Ling, A. Harvey, D. McAteer, I. J. Godwin, B. Szydlowska, A. Griffin, V. Vega-Mayoral, Y. C. Song, A. Seral-Ascaso, V. Nicolosi and J. Coleman, *Adv. Energy Mater.*, 2018, **8**, 1702364.
67 D. O'Suilleabhain, V. Vega-Mayoral, A. G. Kelly, A. Harvey and J. N. Coleman, *ACS Appl. Mater. Interfaces*, 2019, **11**, 8545–8555.

